Journal of Magnetism and Magnetic Materials 528 (2021) 167772

Contents lists available at ScienceDirect

Journal of Magnetism and Magnetic Materials

journal homepage: www.elsevier.com/locate/jmmm

Research articles

Multi-domain ferromagnetic resonance in magnetic van der Waals crystals CrI_3 and $CrBr_3$

Xi Shen [a,b], Haoran Chen [a,b], Yi Li [c,1], Hong Xia [a,b], Fanlong Zeng [a,b], Jia Xu [a,b], Hee Young Kwon [d], Yi Ji [e], Changyeon Won [f], Wei Zhang [c,*], Yizheng Wu [a,b,*]

[a] Department of Physics and State Key Laboratory of Surface Physics, Fudan University, Shanghai 200433, China
[b] Shanghai Research Center for Quantum Sciences, Shanghai 201315, China
[c] Department of Physics, Oakland University, Rochester, MI 48309, USA
[d] Center for Spintronics, Korea Institute of Science and Technology, Seoul 02792, South Korea
[e] Department of Physics and Astronomy, University of Delaware, Newark, DE 19716, USA
[f] Department of Physics, Kyung Hee University, Seoul 130-701, Republic of Korea

ARTICLE INFO

Keywords:
Ferromagnetic resonance
van der Waals crystal
Magnetic domain

ABSTRACT

Two-dimensional (2D) magnetic van der Waals crystals have received great attentions recently owing to their novel electronic and magnetic properties and rich potentials for low-dimensional and high-density spintronic devices. We investigated the magnetization dynamics of CrI_3 and $CrBr_3$ bulk single crystals by utilizing broadband ferromagnetic resonance (FMR) in a frequency range of 1 – 40 GHz and over a wide temperature range of 10 – 300 K. Complex features observed in the FMR spectra are quantitatively described by the multi-domain FMR theory. The minimum resonance frequency f_{min} in FMR spectra was recognized and analyzed as characteristics of the transition of the domain structure. Micromagnetic simulation on the domain structure and spin dynamics explains that the multi-domain structure exists under strong in-plane magnetic field for CrI_3 and $CrBr_3$ and significantly influences the magnetic dynamics properties. Our results also suggest that the linewidths of FMR spectra in CrI_3 and $CrBr_3$ are dominated by the magnetic inhomogeneous broadening.

1. Introduction

Recent interests in two-dimensional (2D) magnetic van der Waals crystals are driven by their rich electronic and optical properties as well as their potential application in future electronics, spintronics, and optoelectronics [1–8]. 2D magnetic layers can be created when an atomic monolayer is exfoliated from a bulk layered magnetic crystal and maintains its magnetic ordering [9–12]. Such attractive magnetic material systems promote studies of new physics in low-dimensional magnetism and enable constructions of novel spintronic heterostructures. In the new family of 2D magnetic layers, chromium trihalides CrX_3 (X = Br or I) is one of the first members that have been found to exhibit magnetism in a single atomic layer [1,13]. A wealth of exotic properties on CrX_3, such as giant tunneling magnetoresistance [14,15], gate- and pressure- tuned interlayer magnetism [16–18], topological-magnetic proximity effect in topologic insulator/CrX_3 heterostructures [19,20], have been reported recently, suggesting CrX_3 as a good candidate to construct future spintronics devices.

Understanding the bulk properties of these layered CrX_3 crystals is an essential step toward creating and comprehending their 2D counterparts. $CrBr_3$ was first confirmed as a magnetic semiconductor in 1960 s [21,22], with a Curie temperature (T_C) of 37 K and the easy axis orienting along the hexagonal c-axis. The magnetism in CrI_3 was later found with a strong anisotropy along the c-axis with T_C of 68 K [23,24]. Magnetic domains in single crystal $CrBr_3$ and CrI_3 foils have been investigated by Lorentz microscope [25], electron microscope [26] and magneto-optic Faraday effect [27,28], and those studies showed the meander, strip, and honeycomb domains could be produced by applying suitable fields during the cooling of the specimen. To cultivate the full potential of the layered magnets for device applications, their magnetic dynamic properties such as spin wave excitations should be investigated in details. It is also crucial to understand their magnetic anisotropy and damping mechanism to provide essential information for applications such as magnetic switching, magnon excitation and quantum

* Corresponding authors.
E-mail addresses: weizhang@oakland.edu (W. Zhang), wuyizheng@fudan.edu.cn (Y. Wu).
[1] Present address: Materials Science Division, Argonne National Laboratory, Lemont, IL 60439, United States.

https://doi.org/10.1016/j.jmmm.2021.167772
Received 26 October 2020; Received in revised form 23 December 2020; Accepted 17 January 2021
Available online 23 January 2021

processing.

Ferromagnetic resonance (FMR) measurement is crucial to characterizing dynamical properties of magnetic materials. There were several reports on the FMR measurements of CrX_3 crystals [22,23,29,30], but the previous studies were limited to narrow-band microwave frequencies without concerning about domain structures inside the samples. Comprehensive studies and theoretical analysis on the frequency-dependent dynamic properties of CrX_3 crystals are still lacking, though they would provide a deeper understanding on the magnetic properties and accurate determination of magnetic parameters of these magnetic van der Waals crystals.

In this work, we performed broadband FMR measurements on high-quality CrI_3 and $CrBr_3$ single-crystal flakes with microwave frequency up to 40 GHz and magnetic field in the flake plane. From strong FMR signals at various temperatures, we characterized the frequency dependence of resonance. Our results clearly demonstrate the influence of multi-domain structure on the magnetic dynamics properties, and the multi-domain FMR model with the field below the anisotropic field can be applied to quantitatively analyze the experimental data. Utilizing the magnetic parameters obtained from the experimental data, we performed micromagnetic simulation and demonstrated the existence of multi-domain structures under strong in-plane field. The simulated resonance spectra quantitatively agree with experimental results. Moreover, our measurements indicate that the linewidth of the uniform FMR mode is mainly attributed to the magnetic inhomogeneous broadening.

2. Experimental and simulation methods

Our studies were performed on high quality CrI_3 and $CrBr_3$ single crystals with (0001) orientation purchased from HQ Graphene company. The bulk crystal samples in FMR measurements usually have the flake shape with the typical lateral size of ~ 0.7 mm and the thickness of ~ 0.1 mm. The magnetic behaviors of the materials are first characterized using a superconducting quantum interference device (SQUID, Quantum Design MPMS 3). Hysteresis loops with magnetic field along the in-plane and out-of-plane direction were measured respectively at various temperatures. From the magnetization measurement, we determine the T_Cs of our CrI_3 and $CrBr_3$ samples are 68 K and 37 K, respectively.

The FMR measurements were performed through a broadband coplanar waveguide (CPW) placed into a Physical Property Measurement System (PPMS, Quantum Design) system. The samples were positioned on the signal line of the CPW waveguide. The magnetic field in the PPMS was applied along the signal line in the CPW plane, thus, it was applied in the flake plane perpendicular to the c-axis of CrI_3 and $CrBr_3$ during the FMR measurements. The transmission parameter S_{21} was measured using a vector network analyzer (R&S ZVA40) with the microwave power fixed at −10 dbm. The microwave frequency f was varied between 1 GHz and 40 GHz, the sample temperature varied from 10 K to above T_C in this study. The samples were loaded into the PPMS system within a few minutes after being mounted onto the microwave holder in a glove box, thus the possible surface decomposition is expected have very limited influence on the magnetic properties of the bulk crystals in our measurements.

In order to understand the origin of resonance modes in details, we performed the micromagnetic simulation to calculate spin structure and the dynamics excitation as a function of the in-plane field. The computational simulation was performed with the modified code package MuMax3 [31]. Since the exchange coupling energy between neighbor Cr spins is 2.7 meV for CrI_3 and 2.4 meV for $CrBr_3$ [32], we used the exchange stiffness constant A_{ex} of 1.2 pJ/m. During the simulation, we chose the experimental values of the perpendicular anisotropy K_z and saturation magnetization M at different temperatures. The damping constant α used in the simulation is 0.01. In order to compare with the experimental bulk system, very thick film systems were simulated with the size of $2 \times 2 \times 0.4\ \mu m^3$ for CrI_3 and $2.4 \times 2.4 \times 0.48\ \mu m^3$ with in-plane periodic boundary condition. The long-range dipolar interaction is considered in the simulation. The calculated domain wall width is about 10 nm, and the wall width in CrI_3 is smaller due to the stronger anisotropy, so the unit cell in the simulation is 2 nm for CrI_3 and 3 nm for $CrBr_3$.

We first simulated the static domain structures of CrI_3 and $CrBr_3$ with the magnetic parameters determined at different temperatures. Then, the field-dependent domain evolutions were simulated while applying an in-plane field. In order to obtain the dynamic properties in the multi-domain systems, we applied an in-plane time-dependent field with a cardinal sine function $\mathrm{sinc}(\pi f_c t)/\pi f_c t$ with a cutoff frequency $\mathrm{off}_c = 80$ GHz [33], and the amplitude of the excitation field was 0.1 mT. The transient dynamics was computed over 20 ns, with the data taken every 10 ps. We obtained the time-dependent perpendicular component of the averaged magnetization, and further calculated the power spectrum density (PSD) through the Fourier transformation, then the resonance peak at each field could be obtained.

3. Results and discussions

Fig. 1(a) and 1(b) show the typical hysteresis loops measured by SQUID for CrI_3 and $CrBr_3$ under the field applied either parallel ($H_{\parallel}$) or perpendicular ($H_{\perp}$) to the crystal flake. The remanence is nearly zero for both CrI_3 and $CrBr_3$, which can be attributed to the multi-domain states [34–36]. At 2 K, the saturation field of CrI_3 is ~ 2.6 T for the $H_{\parallel}$ scan and only ~ 0.2 T for the $H_{\perp}$ scan, in consistent with the strong uniaxial anisotropy in CrI_3 with easy axis along the c-axis perpendicular to the flake plane [23,37,38]. At 80 K (above T_C), the hysteresis loops scanned with $H_{\parallel}$ and $H_{\perp}$ show the identical shape, indicating isotropic magnetic properties above T_C. The measured hysteresis loops of $CrBr_3$ in Fig. 1(b) are very similar to those of CrI_3; the saturation field at 2 K is ~ 0.6 T for the $H_{\parallel}$ scan and ~ 0.2 T for the $H_{\perp}$ scan, thus $CrBr_3$ also contains the magnetic anisotropy perpendicular to the flake with the anisotropy field weaker than that of CrI_3.

Fig. 2(a) shows the typical field-dependent absorption spectra of CrI_3 at 10 K with various microwave frequencies, and the FMR measurement geometry is plotted as an inset. The sample flakes were placed on top of the signal line with a width of 0.36 mm, and the magnetic field H was applied along the signal line parallel to the flake plane, which is in the same geometry for hysteresis loops scan with $H_{\parallel}$. There is no resonance signal for the microwave frequency f less than 22 GHz, and the FMR resonance absorption starts to be observed at ~ 22 GHz. The FMR absorption develops into two peaks for $f > 22$ GHz, and the separation of these two peaks increases with f. In order to better present the evolution of the FMR resonance, we present the measured frequency-dependent

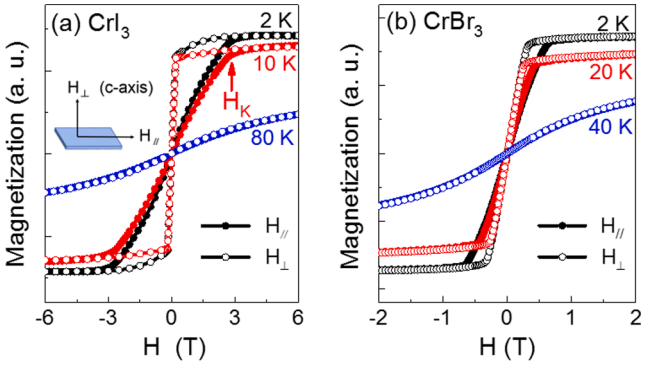

Fig. 1. The typical hysteresis loops at various temperatures for (a) CrI_3 and (b) $CrBr_3$. The magnetization is measured with the field applied either parallel ($H_{\parallel}$, solid circles) or perpendicular to the flake ($H_{\perp}$, open circles). The inset in (a) shows the sketch of the sample with hexagonal c-axis perpendicular to the flack plane.

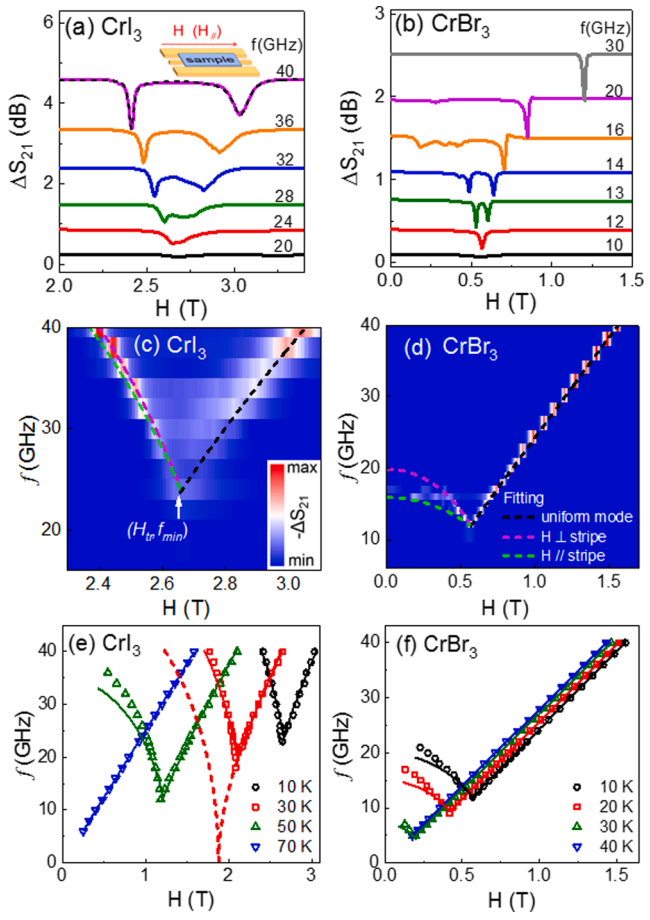

Fig. 2. Typical curves of FMR absorption spectra at 10 K for (a) CrI_3 and (b) $CrBr_3$, the inset in (a) shows the schematic of FMR measurement, the dash line in (a) is the fitting results using Eq. (1) at 40 GHz. The color map of FMR spectra at 10 K for (c) CrI_3 and (d) $CrBr_3$. The dash lines are fitting curves of the uniform mode and the calculated curves using multi-domain FMR theory. The *f*-H_r dispersions at various temperatures for (e) CrI_3 and (f) $CrBr_3$. The solid lines are fitting curves of the uniform mode above H_K and the calculated curves using the multi-domain theory with the field perpendicular to the stripes. The red dash line in (e) is the calculated curve in whole field range using the single domain model with the parameters of CrI_3 at 30 K.

FMR spectra into the color map in Fig. 2(c), which clearly shows that the resonance frequency first decreases with H below a critic field H_{tr} of 2.66 T, then increases with H at higher field, the minimum resonance frequency f_{min} at H_{tr} is ~ 22 GHz. The similar FMR measurement is also performed on $CrBr_3$. As shown in Fig. 2(b), the FMR spectra of $CrBr_3$ at 10 K show similar behavior as those of CrI_3. The color map of measured FMR spectra in Fig. 2(d) shows the critic field H_{tr} of ~ 0.56 T with f_{min} of 12 GHz. For $f > 20$ GHz, there is only a single resonance peak at higher field.

The measured absorption spectra can be well fitted by a Lorentzian function [39–41]

$$\Delta S_{21} = A_L \frac{\Delta H^2}{(H - H_r)^2 + \Delta H^2} + A_D \frac{\Delta H(H - H_r)}{(H - H_r)^2 + \Delta H^2} \quad (1)$$

which is a superposition of the symmetric and anti-symmetric Lorentz line shapes. A_L and A_D are the amplitudes of symmetric and anti-symmetric Lorentz line shape, respectively. The measured FMR spectra in Fig. 2(a) and 2(b) are dominated by the symmetric shape, thus the fitted A_L is always one order larger than A_D. From the fitting, we obtained the resonance field H_r and the linewidth ΔH of the resonance peak. Fig. 2(e) and 2(f) show the fitted *f*-H_r dispersions at different temperatures for CrI_3 and $CrBr_3$ respectively. At high temperature above T_C, there is only one adsorption peak for a fixed microwave frequency, and the resonance frequency linearly increases with the field. At the lower temperature below T_C, the resonance frequency first decreases with the field, then increases at higher field above H_{tr}. Both H_{tr} and f_{min} increase while the temperature decreases.

The *f*-H_r dispersion in typical uniform magnetic systems with uniaxial anisotropy has been well investigated [42–44]. For magnetic field along the hard axis, the resonance frequency of the uniform magnetization procession mode first decreases with the field, and then increases again after reaching the zero value [42,43], as indicated by the red dash line in Fig. 2(e), thus the experimental *f*-H_r dispersion for CrI_3 and $CrBr_3$ cannot be explained using the uniform precession mode. Note that the stripe domains exist in CrI_3 and $CrBr_3$ at the low field state [25–28], such stripe domains can significantly influence the magnetic resonance.

We quantitatively analyzed our FMR results with the multi-domain FMR theory [45] and it well describes our results. As shown in Fig. 3 (a), our analysis is based on the periodic stripe domain structure. The sample consists of two sets of domains with equal volume, and the magnetization in the neighboring domain should have the opposite magnetization component along z-direction, thus there is no net M_z under the in-plane magnetic field. The static field H is applied with the angle φ_H respected to the stripe, and the applied microwave field is perpendicular to H in the plane. The magnetization can be canted by H, and the in-plane projection of magnetization in each domain should be parallel to H. The free energy density is written as [46,47]:

$$E = -\frac{HM}{2}(\sin\theta_1\sin\varphi_1 + \sin\theta_2\sin\varphi_2) + \frac{K_z}{2}(\sin^2\theta_1 + \sin^2\theta_2)$$
$$+\frac{N_x}{2}\frac{M^2}{4}(\sin\theta_1\cos\varphi_1 - \sin\theta_2\cos\varphi_2)^2 + \frac{N_y}{2}\frac{M^2}{4}(\sin\theta_1\sin\varphi_1 - \sin\theta_2\sin\varphi_2)^2$$
$$+\frac{N_z}{2}\frac{M^2}{4}(\cos\theta_1 - \cos\theta_2)^2 + \frac{4\pi}{2}\frac{M^2}{4}(\cos\theta_1 + \cos\theta_2)^2 \quad (2)$$

Here, M represents the saturation magnetization of material, θ_1 and θ_2 represent the out-of-plane angles of domain magnetization, φ_1 and φ_2 represent the in-plane projection angles of magnetization in each domain, K_z is the perpendicular magnetic anisotropy energy density, N_i

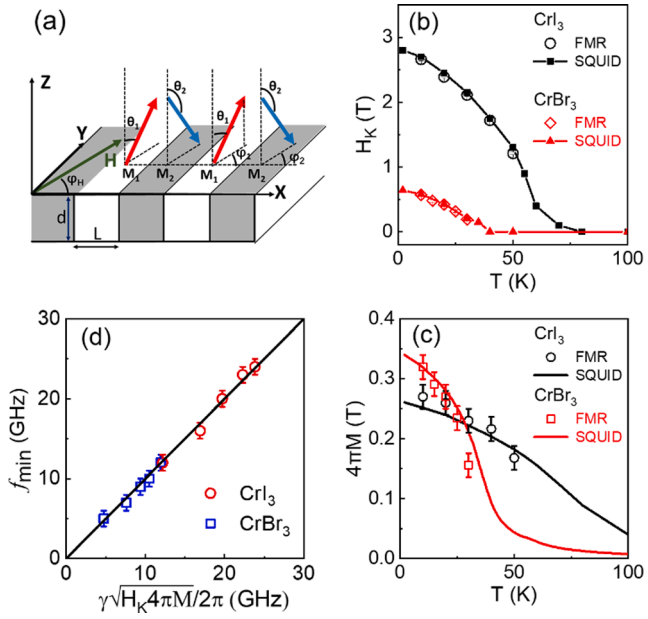

Fig. 3. (a) The illustration of magnetization structures for the stripe domain phase with the in-plane field for the multi-domain FMR calculation. (b) The anisotropic field H_K and (c) the magnetization of CrI_3 and $CrBr_3$ obtained from the FMR and SQUID measurements. (d) The correlation between the experimental values of f_{min} and $\frac{\gamma}{2\pi}\sqrt{H_K \cdot 4\pi M}$. The solid line is calculated by Eq. (6).

(N_x, N_y, N_z) are the demagnetization parameters of each domain with the relation of $N_x + N_y + N_z = 4\pi$. The first term in Eq. (2) is the Zeeman energy, the second term is the perpendicular anisotropy energy, and the other terms include all of the demagnetizing energies. Eq. (2) ignores the energy contribution from the domain wall energy. Usually, the domain wall width is on the order of $\pi\sqrt{A/K_z}$ where A is the exchange stiffness constant, and can be calculated as ~ 10 nm for CrI_3 and $CrBr_3$, which is much smaller than the domain size in the order of 1 μm [25–28]. Therefore, the domain wall energy has the negligible contribution to the total energy, and the effect of domain wall to the multi-domain resonance can be neglected.

Fig. 3(a) also shows that the domain system follows the conditions of $\theta_1 + \theta_2 = \pi$ and $\varphi_1 = \varphi_2 = \varphi_H$, thus at the static equilibrium state, the magnetization angle θ_1 can be determined by the equation $\sin\theta_1 = \frac{H}{H_K - N_z M}$, with $H_K = \frac{2K_z}{M}$ as the anisotropy field. For $H \geq H_K - N_z M$, all the magnetization is aligned in the film plane to form a uniform magnetization state, then the magnetic resonance frequency can be determined by

$$f = \frac{\gamma}{2\pi}\sqrt{H(H - H_K + 4\pi M)} \quad (3)$$

The FMR frequency at the uniform procession mode increases with H. By fitting the experimental f-H_r dispersion at strong field, we can obtain the values of $H_K - 4\pi M$ and the gyromagnetic ratio γ.

For $H < H_K - N_z M$, the FMR frequency depends on the in-plane field angle φ_H and the demagnetization parameters N_i (N_x, N_y, N_z). The demagnetization parameters N_i should depend on the aspect ratio in each domain. Our sample usually has the thickness d in the order of 100 μm, and the stripe domain width L has the order of 1 μm, thus the aspect ratio L/d is on the order of 0.01. In this case, the demagnetization parameters can be simplified as $N_y \sim N_z \sim 0$ and $N_x \sim 4\pi$ [46,47]. Then the resonance frequency f in the multi-domain state depends on φ_H. For $\varphi_H = 0^\circ$ with H⊥stripe, the FMR frequency can be described by

$$f = \frac{\gamma}{2\pi}\sqrt{H_K{}^2 + 4\pi M \cdot H_K - H^2} \quad (4)$$

and for $\varphi_H = 90^\circ$ with H||stripe, the FMR frequency can be described by

$$f = \frac{\gamma}{2\pi}\sqrt{H_K{}^2 + 4\pi M \cdot H^2/H_K - H^2} \quad (5)$$

The relative angle φ_H between stripe domain and the applied field could vary between 0° and 0°, then the corresponding FMR frequency should vary between the values calculated by Eq. (4) and Eq. (5). Note that the FMR frequency decreases with the field in the multi-domain modes, but increases in the uniform procession mode, and all the multi-domain modes and the uniform procession mode cross at the field H_{tr} equal to H_K. As a result, the minimum FMR frequency f_{min} is determined by

$$f_{min} = \frac{\gamma}{2\pi}\sqrt{H_K \cdot 4\pi M} \quad (6)$$

Since we can determine $H_K - 4\pi M$ by fitting the f-H_r dispersion in the uniform procession mode and H_K from H_{tr} in the f-H_r spectra, $4\pi M$ can also be quantified through the resonance measurement. Fig. 3(b) and 3(c) show the determined H_K and $4\pi M$ at different temperatures. The values of H_K and $4\pi M$ also can be quantified from the SQUID data. Our analysis indicates that the magnetization is saturated at H_K while applying the in-plane field $H_{\|}$, thus H_K can be quantified by the saturation field in the hysteresis loops, as indicated by the red arrows in Fig. 1. As shown in Fig. 3(b) and 3(c), the values of H_K and $4\pi M$ determined from FMR experiments agree precisely with the results from the SQUID measurements. The determined values of H_K and $4\pi M$ for CrI_3 at 10 K are ~ 2.66 T and ~ 0.27 T respectively, and those values for $CrBr_3$ at 10 K are H_K ~ 0.56 T and $4\pi M$ ~ 0.32 T, in consistent with the literatures [23,37].

Using Eqs. (4) and (5), the multi-domain resonance modes were quantitatively calculated with the fitting parameters γ, H_K and $4\pi M$. In Fig. 2(c) , the two multi-domain modes with $\varphi_H = 0^\circ$ and 90° are very similar for CrI_3. In Fig. 2(d), the calculated two multi-domain modes are well separated for $CrBr_3$, and the experimental FMR spectra are closer to the $\varphi_H = 0^\circ$ mode than the $\varphi_H = 90^\circ$ mode, indicating that most stripes in $CrBr_3$ are perpendicular to the field. For CrI_3, we also find that the $\varphi_H = 0^\circ$ mode at higher temperature with lower anisotropy is closer to the experimental data. In Fig. 2(e) and 2(f), we also plot the calculated f-H_r dispersion of the $\varphi_H = 0^\circ$ mode, which are in good agreement with the experimental f-H_r dispersions at different temperatures.

Eq. (6) indicates that the lowest resonance frequency f_{min} in FMR spectra is $\frac{\gamma}{2\pi}\sqrt{H_K \cdot 4\pi M}$. Thus, f_{min} can be calculated by Eq. (6) with experimentally determined γ, H_K and $4\pi M$. Fig. 3(d) demonstrates the calculated f_{min}s by Eq. (6) are nearly same as the experimental values. Magnetic dynamic studies on the layered ferromagnetic crystals such as $Cr_2Ge_2Te_6$ have been reported recently [48,49] and FMR spectra with a f_{min} were also observed by applying the magnetic field parallel to the ab-plane, though those studies generally focused on the single-domain resonance mode without examining the multi-domain resonance mode. Our measurements and analysis convince that the multi-domain FMR theory is valid to describe the FMR spectra in layered 2D magnetic van der Waals crystals.

Micromagnetic simulation further demonstrates that the multi-domain FMR theory quantitatively describes the experimental results. Fig. 4(a) shows the typical domain structure calculated with the magnetic parameters $K_z = 0.287$ MJ/m^3 and $M = 0.216$ MA/m, which are experimentally determined from CrI_3 at 10 K. We simulated the magnetic domains by gradually cooling the film from the temperature above T_C. The static domain at zero temperature shows the labyrinth structure, and the width of the domain is ~ 300 nm with the domain wall width of ~ 10 nm. Then, we gradually apply the in-plane field along the × axis, and Fig. 4(b-d) show the field-dependent evolution of domain structures. Fig. 4(e) shows the representative line profiles at different fields demonstrating the canting of magnetization. Our simulation shows that the multi-domain structure persists in the in-plane field up to H_K, which is 2.66 T for CrI_3 at 10 K. Fig. 4(f-i) present the calculated domain structures at different fields with $K_z = 0.072$ MJ/m^3 and $M = 0.256$ MA/m measured in $CrBr_3$ at 10 K, and the typical width is ~ 250 nm for domains and ~ 15 nm for domain walls. The simulated domain size in $CrBr_3$ is also in the same order of the experimental domain images measured by scanning magnetometry using a single-electron spin of a nitrogen vacancy center in a diamond probe [50]. We also calculated the field-dependent magnetization angle θ_1 of two systems, as plotted in Fig. 4(j). The simulated field dependent θ_1 agrees very well with the theoretical relation of $\theta_1 = \arcsin(H/H_K)$ from the multi-domain theory.

Usually, it is expected that the external field can align the stripe domains with the Bloch-type wall to reduce the total energy [51]. Fig. 4 (a) and 4(f) show that the domain walls at zero field are also Bloch-type. After applying an in-plane field above 0.1 T, the magnetization inside the domain walls is aligned along the field direction, but the domain orientation does not. This may be attributed to that the Zeeman energy in the narrow domain walls is not strong enough to rotate the stripe orientation. If the system is cooled under a field from the paramagnetic state above T_C, the perfect alignment of stripes along the field can be achieved.

The magnetic dynamic properties of the CrI_3 and $CrBr_3$ system were further calculated. Fig. 5(a) presents the typical simulated PSD spectra using the parameters of CrI_3 measured at 10 K. Fig. 5(b) shows the color map of PSD of excitations as a function of H, which is very similar to the experimental results in Fig. 2(c), and the calculated f-H_r dispersions for the multi-domain mode and the uniform procession mode agree well with the simulation results.

The similar simulation was also performed with the parameters of $CrBr_3$ measured at 10 K as shown in Fig. 5(c). Different with the

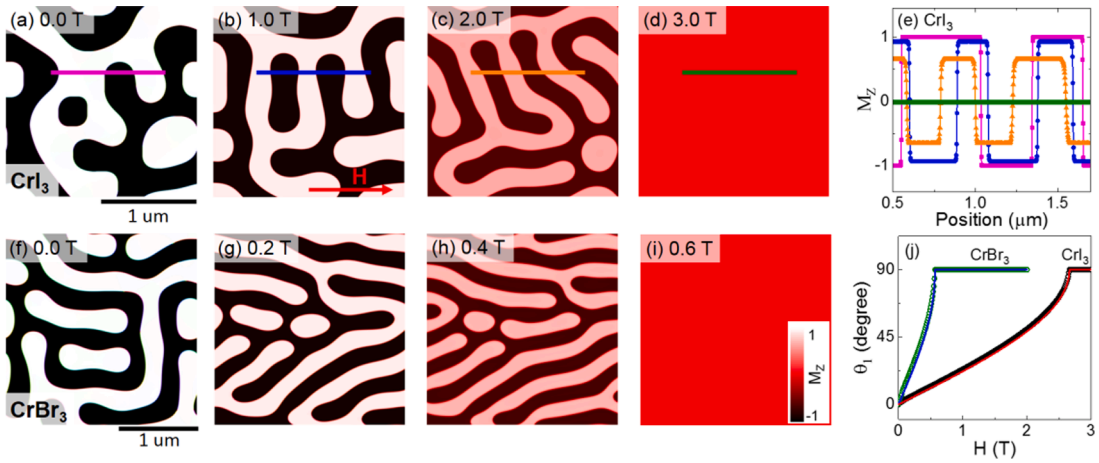

Fig. 4. The simulated domain structures under different in-plane fields using the extracted parameters of (a)-(d) CrI_3 and (f)-(i) $CrBr_3$ at 10 K. The color bar of M_Z is displayed in (i). (e) Line profiles across the lines shown in (a)-(d). (j) The field dependent magnetization orientation angle θ_1 obtained from the simulated domain patterns (open circles) and from the analytical relation (solid lines).

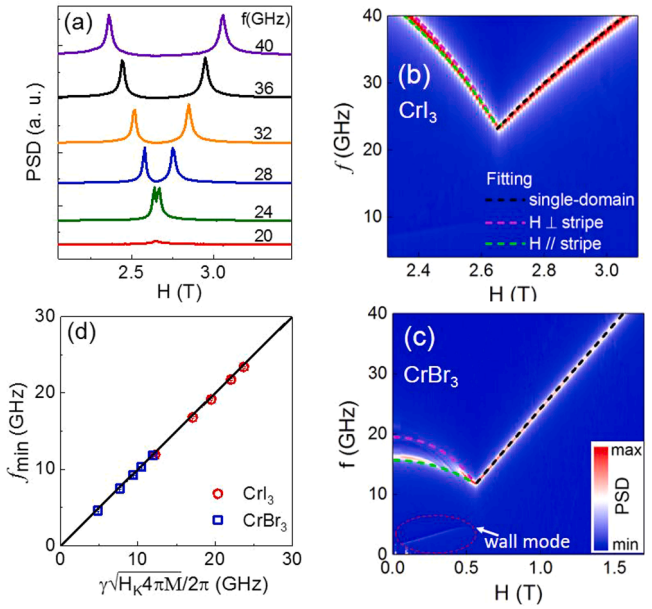

Fig. 5. (a) The simulated PSD curves as a function of field with different frequencies using the magnetic parameters for CrI_3 at 10 K. The color map of simulated FMR spectra utilizing the magnetic parameters for (b) CrI_3 and (c) $CrBr_3$ at 10 K. The dashed lines are the calculated results of the multi-domain FMR modes and the uniform mode. The dashed circle in (c) highlights the domain wall resonance mode. (d) The correlation between f_{min} in the simulations and $\frac{\gamma}{2\pi}\sqrt{H_K \cdot 4\pi M}$. The solid line is calculated by Eq. (6).

experimental FMR spectra in Fig. 2(d), the simulated spectra in the multi-domain mode is closer to the theoretical model with the stripe parallel to H, in consistent with the domain pattern shown in Fig. 4(f). The stripe domains are not fully aligned with H, thus some intermediate resonance modes could also be involved. Beside the resonance mode in the domain region, we found an additional resonance mode located in the domain wall region, as highlighted by the dashed circle in Fig. 5(c). Our simulations show that the domain size increases while increasing the film thickness, and the relative intensity of domain wall resonance mode decreases accordingly. Therefore, it is reasonable that such domain wall resonance mode could not be observed experimentally, because the thickness of the film used in the experiment is in the order of ~ 100 μm.

Fig. 5(b) and 5(c) show the minimum resonance frequency f_{min} of ~ 22 GHz for CrI_3 and of ~ 12 GHz for $CrBr_3$. We performed the simulations with the magnetic parameters measured at different temperatures, and all the simulated f-H_r dispersions agree well with the experimental data. From the simulated FMR spectra, f_{min} was determined, which was almost same as the value calculated by $\frac{\gamma}{2\pi}\sqrt{H_K \cdot 4\pi M}$ as shown in Fig. 5 (d). We found that the simulated spectra change with the film thickness, but they are gradually stabilized for the thickness above 300 nm, thus in order to compare with the experimental system more precisely, the simulated film system in this study would be thicker than 400 nm.

Besides the f-H_r dispersions, the linewidth ΔH of the FMR adsorption peaks was analyzed. Fig. 6(a) presents the evolution of the FMR absorption curves of the uniform procession mode for CrI_3 at 30 K, showing that the linewidth decreases with the increasing f. The typical FMR absorption curves for $CrBr_3$ at 20 K, shown in Fig. 6(b), indicates that the linewidth is nearly independent of f. All the presented absorption curves

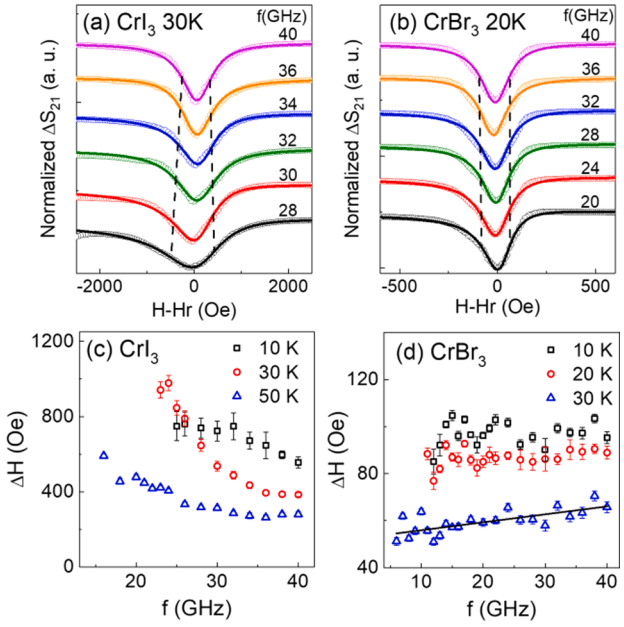

Fig. 6. The FMR absorption curves in the uniform mode at various f for (a) CrI_3 and (b) $CrBr_3$. The open circles are experimental data and the solid lines are the fitting curves using the Lorentzian function Eq. (1). The dash lines are guide for the change of the linewidth. The f-dependent linewidth ΔH of the uniform procession mode for (c) CrI_3 and (d) $CrBr_3$ measured at different temperatures. The solid line in (d) is from a linear fitting.

are from the uniform mode, so the applied field is strong enough to align the magnetization in the film plane. Fig. 6(c) and 6(d) show the measured *f*-dependent ΔH at different temperatures for CrI_3 and $CrBr_3$. ΔH of CrI_3 decreases with *f* at all the temperatures, but ΔH of $CrBr_3$ has little dependence on *f* and slightly increases with *f* at 30 K.

It is well known that the total linewidth at the saturation state has three major contributions [52–54]: intrinsic Gilbert damping, magnetic inhomogeneous and two-magnon scattering. The intrinsic Gilbert damping is an important magnetic dynamic property, and the linewidth induced by the intrinsic Gilbert damping has a linear dependence on *f* from which the damping constant α can be extracted. In the magnetic system with strong uniaxial anisotropy, two-magnon scattering process does not exist for the field along the hard axis [54,55]. Then, the decreasing behavior of the ΔH- *f* relation should be attributed to the magnetic inhomogeneous broadening, which can be suppressed by the strong field. Although the applied field is stronger than H_K and aligns the magnetization in the film plane, there are still strong magnetic frustration existing in 2D magnetic materials. As shown in Fig. 1, the total magnetization still gradually increases with the field above H_K due to the field suppression on magnetic frustration. The strong effect on the linewidth due to the magnetic inhomogeneous prohibits the determination of intrinsic damping constant. The linewidth of $CrBr_3$ at 30 K shows a linear dependency with *f* in Fig. 6(d), indicating a Gilbert-type damping mechanism with a weaker anisotropy in $CrBr_3$. From the linear fitting, we obtained the damping constant of 0.009 ± 0.002. This value only provides the lower limit of the intrinsic damping constant, since the effect on the linewidth from magnetic inhomogeneous still exists at this condition. Our results suggest that the magnetic frustration in 2D magnetic materials would be suppressed under stronger field, and microwave with much higher frequency is required to obtain the correct intrinsic Gilbert damping constant.

4. Conclusion

In summary, magnetic dynamic properties of single crystal CrI_3 and $CrBr_3$ have been characterized systematically using the broadband FMR measurements and micromagnetic simulation. The experiment data are well described by the multi-domain FMR theory. The magnetic parameters such as magnetic moment and magnetic anisotropy are fitted from the theory, and they have a good agreement with SQUID results. Magnetic domain structures and FMR spectra for CrI_3 and $CrBr_3$ with in-plane magnetic field were simulated, and the multi-domain FMR model is validated by the detailed comparison between simulations and experiments. Our results also suggest that the linewidth of FMR spectra are dominated by the magnetic inhomogeneous broadening, and the stronger field is required to correctly extract the intrinsic damping constant. The rich information and comprehensive analysis on magnetization dynamics acquired in this study are essential for understanding the intrinsic magnetic properties of 2D magnets and related heterostructures.

CRediT authorship contribution statement

Xi Shen: Investigation, Data curation, Formal analysis, Methodology, Writing - original draft. **Haoran Chen:** Software, Methodology. **Yi Li:** Formal analysis, Methodology, Visualization. **Hong Xia:** Software, Methodology. **Fanlong Zeng:** Visualization. **Jia Xu:** Visualization. **Hee Young Kwon:** Formal analysis, Methodology. **Yi Ji:** Writing - review & editing. **Changyeon Won:** Formal analysis, Methodology. **Wei Zhang:** Methodology, Writing - review & editing. **Yizheng Wu:** Conceptualization, Methodology, Writing - review & editing.

Declaration of Competing Interest

The authors declare that they have no known competing financial interests or personal relationships that could have appeared to influence the work reported in this paper.

Acknowledgements

We acknowledge helpful discussions with Prof. Jiang Xiao and Prof. Bret Heinrich. The work at Fudan University was supported by National Key Research and Development Program of China (Grant No. 2016YFA0300703), National Natural Science Foundation of China (Grants No. 11734006, No. 11974079), and Project supported by Shanghai Municipal Science and Technology Major Project (Grant No. 2019SHZDZX01). Work at Khung Hee University was supported by the NRF funded by the Korean Government (NRF-2018R1D1A1B07047114). Work at Korea Institute of Science and Technology was supported by the Basic Science Research Program through the National Research Foundation of Korea (NRF) funded by the Ministry of Education (NRF-2019R1A6A3A01091209).

References

[1] B. Huang, G. Clark, E. Navarro-Moratalla, D.R. Klein, R. Cheng, K.L. Seyler, D. Zhong, E. Schmidgall, M.A. McGuire, D.H. Cobden, W. Yao, D. Xiao, P. Jarillo-Herrero, X. Xu, Layer-dependent ferromagnetism in a van der Waals crystal down to the monolayer limit, Nature 546 (2017) 270.
[2] C. Gong, L. Li, Z. Li, H. Ji, A. Stern, Y. Xia, T. Cao, W. Bao, C. Wang, Y. Wang, Z. Q. Qiu, R.J. Cava, S.G. Louie, J. Xia, X. Zhang, Discovery of intrinsic ferromagnetism in two-dimensional van der Waals crystals, Nature 546 (2017) 265.
[3] Z. Fei, B. Huang, P. Malinowski, W. Wang, T. Song, J. Sanchez, W. Yao, D. Xiao, X. Zhu, A.F. May, W. Wu, D.H. Cobden, J.-H. Chu, X. Xu, Two-dimensional itinerant ferromagnetism in atomically thin Fe3GeTe2, Nat. Mater. 17 (2018) 778.
[4] K.S. Burch, D. Mandrus, J.-G. Park, Magnetism in two-dimensional van der Waals materials, Nature 563 (2018) 47.
[5] C. Gong, X. Zhang, Two-dimensional magnetic crystals and emergent heterostructure devices, Science 363, 706 (2019) eaav4450.
[6] M. Gibertini, M. Koperski, A.F. Morpurgo, K.S. Novoselov, Magnetic 2D materials and heterostructures, Nat. Nanotech. 14 (2019) 408.
[7] J. Sklenar and W. Zhang, Self-hybridization and tunable magnon-magnon coupling in van der Waals synthetic magnets, arXiv:2008.01298 (2020).
[8] J.-F. Dayen, S.J. Ray, O. Karis, I.J. Vera-Marun, M.V. Kamalakar, Two-dimensional van der Waals spinterfaces and magnetic-interfaces, Applied Physics Reviews 7 (2020), 011303.
[9] A.K. Geim, I.V. Grigorieva, Van der Waals heterostructures, Nature 499 (2013) 419.
[10] H.J. Conley, B. Wang, J.I. Ziegler, R.F. Haglund Jr., S.T. Pantelides, K.I. Bolotin, Bandgap Engineering of Strained Monolayer and Bilayer MoS2, Nano Lett. 13 (2013) 3626.
[11] M. Bonilla, S. Kolekar, Y. Ma, H.C. Diaz, V. Kalappattil, R. Das, T. Eggers, H. R. Gutierrez, P. Manh-Huong, M. Batzill, Strong room-temperature ferromagnetism in VSe2 monolayers on van der Waals substrates, Nat. Nanotech. 13 (2018) 289.
[12] X. Zhang, A. Chen, Z. Zhou, High-throughput computational screening of layered and two-dimensional materials, Wires. Comput. Mol. Sci. 9 (2019), e1385.
[13] Z. Zhang, J. Shang, C. Jiang, A. Rasmita, W. Gao, T. Yu, Direct Photoluminescence Probing of Ferromagnetism in Monolayer Two-Dimensional CrBr 3, Nano Lett. 19 (2019) 3138.
[14] T. Song, X. Cai, M.-W.-Y. Tu, X. Zhang, B. Huang, N.P. Wilson, K.L. Seyler, L. Zhu, T. Taniguchi, K. Watanabe, M.A. McGuire, D.H. Cobden, D. Xiao, W. Yao, X. Xu, Giant tunneling magnetoresistance in spin-filter van der Waals heterostructures, Science 360 (2018) 1214.
[15] Z. Wang, I. Gutierrez-Lezama, N. Ubrig, M. Kroner, M. Gibertini, T. Taniguchi, K. Watanabe, A. Imamoglu, E. Giannini, A.F. Morpurgo, Very large tunneling magnetoresistance in layered magnetic semiconductor CrI3, Nat. Commun. 9 (2018) 2516.
[16] S. Jiang, J. Shan, K.F. Mak, Electric-field switching of two-dimensional van der Waals magnets, Nat. Mater. 17 (2018) 406.
[17] S. Jiang, L. Li, Z. Wang, K.F. Mak, J. Shan, Controlling magnetism in 2D CrI3 by electrostatic doping, Nat. Nanotech. 13 (2018) 549.
[18] B. Huang, G. Clark, D.R. Klein, D. MacNeill, E. Navarro-Moratalla, K.L. Seyler, N. Wilson, M.A. McGuire, D.H. Cobden, D. Xiao, W. Yao, P. Jarillo-Herrero, X. Xu, Electrical control of 2D magnetism in bilayer CrI3, Nat. Nanotech. 13 (2018) 544.
[19] Y. Hou, J. Kim, R. Wu, Magnetizing topological surface states of Bi2Se3 with a CrI3 monolayer, Sci. Adv. 5 (2019) eaaw1874.
[20] P. Li, J. Yu, J. Xu, L. Zhang, K. Huang, Topological-magnetic proximity effect in Sb2Te3/CrI3 heterostructures, Physica B 573 (2019) 77.
[21] I. Tsubokawa, On the Magnetic Properties of a Crbr3 Single Crystal, J. Phys. Soc. Jpn. 15 (1960) 1664.
[22] J.F. Dillon, Ferromagnetic Resonance in Crbr3, J. Appl. Phys. 33 (1962) 1191.
[23] J.F. Dillon, C.E. Olson, Magnetization Resonance and Optical Properties of Ferromagnet Cri3, J. Appl. Phys. 36 (1965) 1259.

[24] M.A. McGuire, H. Dixit, V.R. Cooper, B.C. Sales, Coupling of Crystal Structure and Magnetism in the Layered, Ferromagnetic Insulator CrI3, Chem. Mater. 27 (2015) 612.
[25] O. Bostanjoglo, W. Vieweger, Low-Temperature Lorentz Microscopy on Weak Ferromagnetics, Phys. Status Solidi 32 (1969) 311.
[26] Matricar.Vr, W.G. Lehmann, N. Kitamura, J. Silcox, Electron Microscope Observations of Ferromagnetic Domains in Chromium Tribromide, J. Appl. Phys. 38 (1967) 1297.
[27] M. Grundler, B. Kuhlow, M. Lambeck, High-Resolution Light-Optical Observation of Magnetic Domain Structures in Crbr3, Phys. Lett. A **A** 33 (1970) 285.
[28] B. Kuhlow, M. Lambeck, Magnetic Domain-Structures in Crbr3, Physica B & C 80 (1975) 365.
[29] D.L. Huber, M.S. Seehra, Contribution of Spin-Phonon Interaction to Paramagnetic-Resonance Linewidth of Crbr3, J. Phys. Chem. Solids 36 (1975) 723.
[30] V.A. Alyoshin, V.A. Berezin, V.A. Tulin, Rf susceptibility of single-crystal CrBr 3 near the Curie temperature, Phys. Rev. B 56 (1997) 719.
[31] A. Vansteenkiste, J. Leliaert, M. Dvornik, M. Helsen, F. Garcia-Sanchez, B. Van Waeyenberge, The design and verification of MuMax3, AIP Adv. 4 (2014), 107133.
[32] L. Webster, J.-A. Yan, Strain-tunable magnetic anisotropy in monolayer CrCl3, CrBr 3, and CrI3, Phys. Rev. B 98 (2018), 144411.
[33] J.-V. Kim, F. Garcia-Sanchez, J. Sampaio, C. Moreau-Luchaire, V. Cros, A. Fert, Breathing modes of confined skyrmions in ultrathin magnetic dots, Phys. Rev. B 90 (2014), 064410.
[34] B. Niu, T. Su, B.A. Francisco, S. Ghosh, F. Kargar, X. Huang, M. Lohmann, J. Li, Y. Xu, T. Taniguchi, K. Watanabe, D. Wu, A. Balandin, J. Shi, Y.-T. Cui, Coexistence of Magnetic Orders in Two-Dimensional Magnet CrI3, Nano Lett. 20 (2020) 553.
[35] A.S. Westover, K. Chesnel, K. Hatch, P. Salter, O. Hellwig, Enhancement of magnetic domain topologies in Co/Pt thin films by fine tuning the magnetic field path throughout the hysteresis loop, J. Magn. Magn. Mater. 399 (2016) 164.
[36] J.E. Davies, O. Hellwig, E.E. Fullerton, G. Denbeaux, J.B. Kortright, K. Liu, Magnetization reversal of Co/Pt multilayers: Microscopic origin of high-field magnetic irreversibility, Phys. Rev. B 70 (2004), 224434.
[37] N. Richter, D. Weber, F. Martin, N. Singh, U. Schwingenschloegl, B.V. Lotsch, M. Klaeui, Temperature-dependent magnetic anisotropy in the layered magnetic semiconductors CrI3 and CrBr 3, Phys. Rev. Mater. 2 (2018), 024004.
[38] J. Vanherck, C. Bacaksiz, B. Soree, M.V. Milosevic, W. Magnus, 2D ferromagnetism at finite temperatures under quantum scrutiny, Applied Physics Letters 117 (2020), 052401.
[39] G. Counil, J.V. Kim, T. Devolder, C. Chappert, K. Shigeto, Y. Otani, Spin wave contributions to the high-frequency magnetic response of thin films obtained with inductive methods, J. Appl. Phys. 95 (2004) 5646.
[40] G. Counil, J.V. Kim, K. Shigeto, Y. Otani, T. Devolder, P. Crozat, H. Hurdequint, C. Chappert, Inductive measurement of the high frequency permeability of a Permalloy thin film, J. Magn. Magn. Mater. 272 (2004) 290.
[41] C. Bilzer, T. Devolder, P. Crozat, C. Chappert, S. Cardoso, P.P. Freitas, Vector network analyzer ferromagnetic resonance of thin films on coplanar waveguides: Comparison of different evaluation methods, J. Appl. Phys. 101 (2007), 074505.
[42] T.E. Hasty, L.J. Boudreaux, Ferromagnetic Resonance in Thin Magnetic Films at Radio Frequencies, J. Appl. Phys. 32 (1961) 1807.
[43] M. Farle, Ferromagnetic resonance of ultrathin metallic layers, Rep. Prog. Phys. 61 (1998) 755.
[44] I. Neudecker, G. Woltersdorf, B. Heinrich, T. Okuno, G. Gubbiotti, C.H. Back, Comparison of frequency, field, and time domain ferromagnetic resonance methods, J. Magn. Magn. Mater. 307 (2006) 148.
[45] J. Smit, H.G. Beljers, Ferromagnetic resonance absorption in BaFe12O19, a highly anisotropic crystal, Philips Res. Rep. 10 (1955) 113.
[46] J.O. Artman, S.H. Charap, Ferromagnetic-Resonance in Periodic Domain-Structures, J. Appl. Phys. 49 (1978) 1587.
[47] F.J. Rachford, P. Lubitz, C. Vittoria, Microwave Resonance and Propagation in Nonsaturated Ferromagnetic Media. 1. Magnetic-Resonance in Single-Crystal Ferrite Platelets, J. Appl. Phys. 53 (1982) 8940.
[48] X. Zhang, Y. Zhao, Q. Song, S. Jia, J. Shi, W. Han, Magnetic anisotropy of the single-crystalline ferromagnetic insulator Cr2Ge2Te6, Jpn. J. Appl. Phys. 55 (2016), 033001.
[49] S. Khan, C.W. Zollitsch, D.M. Arroo, H. Cheng, I. Verzhbitskiy, A. Sud, Y.P. Feng, G. Eda, H. Kurebayashi, Spin dynamics study in layered van der Waals single-crystal Cr2Ge2Te6, Phys. Rev. B 100 (2019), 134437.
[50] Q.-C. Sun, T. Song, E. Anderson, T. Shalomayeva, J. Förster, A. Brunner, T. Taniguchi, K. Watanabe, J. Gräfe, R. Stöhr, X. Xu, and J. Wrachtrup, Magnetic domains and domain wall pinning in two-dimensional ferromagnets revealed by nanoscale imaging, arXiv:2009.13440v1 (2020).
[51] Y.Z. Wu, A.K. Schmid, M.S. Altman, X.F. Jin, Z.Q. Qiu, Spin-dependent Fabry-Perot interference from a Cu thin film grown on fcc Co(001), Phys. Rev. Lett. 94 (2005), 027201.
[52] J. Lindner, K. Lenz, E. Kosubek, K. Baberschke, D. Spoddig, R. Meckenstock, J. Pelzl, Z. Frait, D.L. Mills, Non-Gilbert-type damping of the magnetic relaxation in ultrathin ferromagnets: Importance of magnon-magnon scattering, Phys. Rev. B 68 (2003), 060102.
[53] Y. Chen, M.J. Nedoroscik, A.L. Geiler, C. Vittoria, V.G. Harris, Perpendicularly oriented polycrystalline BaFe11.1Sc0.9O19 hexaferrite with narrow FMR linewidths, J. Am. Ceram. Soc. 91 (2008) 2952.
[54] K. Zakeri, J. Lindner, I. Barsukov, R. Meckenstock, M. Farle, U. von Hoersten, H. Wende, W. Keune, J. Rocker, S.S. Kalarickal, K. Lenz, W. Kuch, K. Baberschke, Z. Frait, Spin dynamics in ferromagnets: Gilbert damping and two-magnon scattering, Phys. Rev. B 76 (2007), 104416.
[55] M.J. Hurben, C.E. Patton, Theory of two magnon scattering microwave relaxation and ferromagnetic resonance linewidth in magnetic thin films, J. Appl. Phys. 83 (1998) 4344.